Computed Tomography-Based Spectral Imaging For Fluorescence Microscopy

Bridget K. Ford,* Curtis E. Volin,* Sean M. Murphy,† Ronald M. Lynch,† and Michael R. Descour*
*Optical Sciences Center and †Departments of Physiology and Pharmacology, University of Arizona, Tucson, Arizona 85724 USA

ABSTRACT The computed tomography imaging spectrometer (CTIS) is a non-scanning instrument capable of simultaneously acquiring full spectral information (450–750 nm) from every position element within its field of view (75 μm $\times$ 75 μm). The current spatial and spectral sampling intervals of the spectrometer are 1.0 μm and 10 nm, respectively. This level of resolution is adequate to resolve signal responses from multiple fluorescence probes located within individual cells or different locations within the same cell. Spectral imaging results are presented from the CTIS combined with a commercial inverted fluorescence microscope. Results demonstrate the capability of the CTIS to monitor the spatiotemporal evolution of pH in rat insulinoma cells loaded with SNARF-1. The ability to analyze full spectral information for two-dimensional (x, y) images allows precise evaluation of heterogeneous physiological responses within cell populations. Due to low signal levels, integration times up to 2 s were required. However, reasonable modifications to the instrument design will provide higher system transmission efficiency with increased temporal and spatial resolution. Specifically, a custom optical design including the use of a larger format detector array is under development for a second-generation system.

INTRODUCTION

Fluorescence microscopy has developed into a powerful analytical tool in such areas as biology, cell physiology, and medicine (Wang and Herman, 1996). The basis for this power is the development of stable and sensitive analysis devices and fluorescent and luminescent probes (Haugland, 1999; Mason, 1999). Although current technology affords the opportunity to view many biological processes, the full advantage of fluorescence microscopy with simultaneous high temporal, spectral, and spatial resolution is just now fully emerging.

The objective of imaging spectrometry is to measure the proportions of colors associated with narrow and contiguous spectral bands at every position in an imaging instrument's field of view (FOV). The resultant data set is referred to by several names: an object cube, an image cube, a hypercube, or a data cube. Instrumental techniques currently available to acquire an object cube are 1) a filtered camera or multiple cameras, each with its own spectral filter (Wiegmann et al., 1993; Garini et al., 1999); 2) a monochromator configured for imaging, that is, equipped with an imaging array in the exit-slit plane (Eng et al., 1989; Richmond et al., 1997); 3) a Fourier-transform spectrometer equipped with an imaging array (Garini et al., 1999); 4) a tunable illumination source (Zangaro et al., 1996; Zeng et al., 1999); 5) a rotating Risley prism chromatomograph (Mooney et al., 1997); and 6) an acousto-optic tunable filter (AOTF) or liquid-crystal tunable filter (LCTF) combined with a CCD camera (Morris et al., 1994; Wachman et al., 1997; Ornberg et al., 1999). These approaches all require scanning in position or in wavelength in order to record the entire (x, y, λ) object cube. Alternatively, rather than acquiring full spectral information, data can be recorded over a limited region of the spectrum (Wiegmann et al., 1993).

In this paper a computed-tomography imaging spectrometer (CTIS) is described. The CTIS takes advantage of spatial and spectral multiplexing to avoid the need for scanning while maintaining high spectral and spatial resolution over the visible spectrum. The ability of the CTIS to simultaneously acquire data over a broad spectral range at precise spatial positions offers several benefits over existing systems. These benefits include spatial co-registration of spectral images and the possibility of high temporal resolution when the CTIS is coupled to a camera with a fast read-out rate. The current temporal sampling rate of the CTIS falls within the required range for many physiological experiments (0.01–2 s) and the potential temporal resolution is limited only by the detector read-out rate and the signal-to-noise ratio on the array.

The CTIS acquires a continuous fluorescence spectrum (e.g., 450–750 nm) at every pixel so that two-dimensional (2D) images composed of signals from one or multiple fluorescence reporter probes can be acquired simultaneously. This may be of particular importance because analysis of contiguously sampled spectra provides a sensitive approach to correct for probe-independent artifacts, dye-dye interactions, and the cross-sensitivity of probes for multiple factors (Martinez-Zaguilán et al., 1996a, b). In the case of analyzing a single probe, shifts in a probe's spectrum often occur when it interacts with cellular constituents or is trapped within subcellular compartments (Martinez-Zaguilán et al., 1996b). For example, the peak fluorescence emission wavelength may shift corresponding to the ion bound and unbound forms of the probe. Therefore, a ratio of the intensities at two peak emission wavelengths provides precise information about the relative concentration of the

Received for publication 30 June 2000 and in final form 6 November 2000.
Address reprint requests to Bridget K. Ford, Optical Sciences Center, University of Arizona, 1630 E. University Blvd., Tucson, AZ 85721. Tel.: 520-626-7212; Fax: 520-621-3389; E-mail: bford@u.arizona.edu.

0006-3495/01/02/986/08 $2.00

ions (Mason, 1999). The accuracy of such ratiometric calculations is improved by removing the need for post-registration of spectral images. In addition, background fluorescence due to endogenous fluorophores can be significant, and identification of spectral overlap between the background- and probe-specific signals enhances the accuracy of the measurement in such cases (Eng, 1989).

Furthermore, during the course of many physical responses (e.g., hormone secretion, muscle contraction), several cellular parameters may change either simultaneously or in sequence (e.g., Richmond et al., 1997). Because many tissues are heterogeneous with respect to the time course of activation at the cellular level, it is critical to analyze multiple parameters in individual cells with reasonable spatial and temporal resolution. A test of the CTIS will be in applications where cells are loaded with multiple probes for simultaneous analysis of several physiological processes. In this case, spectral data provide precise determination of probe function that is required to rule out probe-probe interactions that can severely influence probe sensitivity and selectivity (Martinez-Zaguilán et al., 1996a, b). Moreover, in the case where probe spectra overlap to a significant degree, spectral line analysis protocols can be utilized to precisely evaluate the signal from the individual probes, which would be impossible if signal responses were monitored over only a few selective wavelengths (Schröck et al., 1996). Thus, with continued development of the CTIS system, the ability to obtain full spectral data will enhance the accuracy and reliability of physiological measurements.

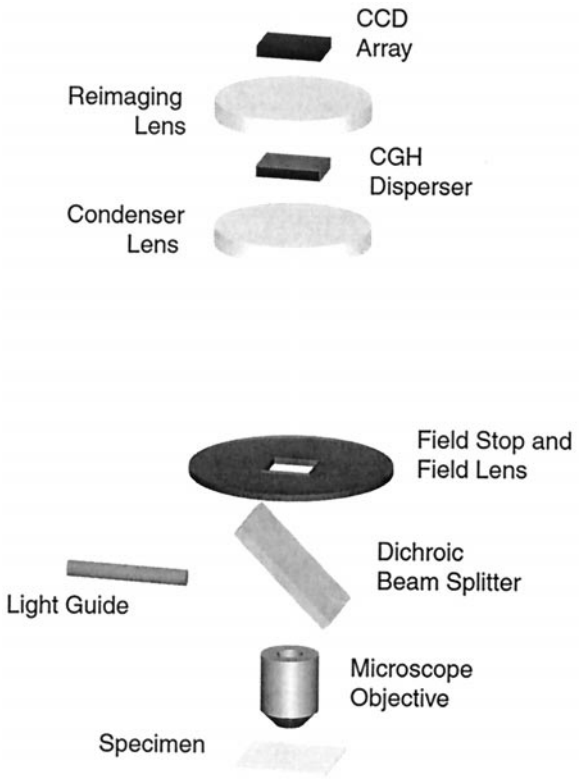

FIGURE 1 Schematic layout of the CTIS microscope combination. In fluorescence imaging experiments, the bare-necessities fore-optics subsystem consists of a light guide from an excitation source, a dichroic beam splitter, and a microscope objective. Distances are not to scale. See text for details.

INSTRUMENT DESCRIPTION

The CTIS microscope consists of two optical subsystems: an interchangeable fore-optics subsystem and the CTIS subsystem. Within the context of this paper, the fore-optics subsystem consists of a standard inverted fluorescence microscope (Olympus IMT-2) equipped with a 100 W mercury lamp as the illumination source. Fig. 1 schematically illustrates the two subsystems of a complete CTIS microscope. For the imaging experiments described herein, an Olympus 60× 1.4 NA objective was used to collect light from the sample, and one of two filter cubes was utilized to reflect the excitation light to the sample and transmit emission light to the CTIS. During the SNARF-1 (free acid) calibration and the microsphere imaging experiments, a single excitation wavelength was selected with a 10-nm bandpass filter centered at 490 nm. The dichroic mirror transmitted >50% of incident emission light above 505 nm. For the SNARF-1 (in situ) calibration and successive pH experiments, the excitation light was centered at 520 nm with a 15-nm bandpass filter to provide more optimal excitation of the SNARF-1. The dichroic mirror in this case passed 50% of the incident emission above 550 nm. An eyepiece (6.7×) at the side photo port of the microscope forms the intermediate image at the field stop of the CTIS subsystem. Thus, a single imaging eyepiece is the only optical element required for adapting the CTIS subsystem to a standard microscope.

The CTIS subsystem includes a field stop, collimator and re-imaging lenses, a computer-generated-hologram (CGH) disperser, and a CCD detector array. The CTIS is constructed with commercial optics, with the exception of the CGH disperser. The disperser is designed to produce a 7 × 7 array of diffraction orders. In designing the CGH, the sum of diffraction efficiencies (η_{tot}) associated with the 49 diffraction orders is maximized such that a maximum fraction of the light collected by the microscope objective is detected. Measurements of η_{tot} have been as high as 78% (Descour et al., 1997a). In order to maintain the same signal and thus the same signal-to-noise ratio across the CCD array, the disperser was designed so that the diffraction efficiency $\eta(\lambda)$ increases in higher diffraction orders to compensate for the increasing dispersion.

In modeling the function of the CTIS, the (x, y, λ) object cube is interpreted as a collection of smaller volume elements, voxels $(\Delta x, \Delta y, \Delta\lambda)$. The CTIS maps the signal from each voxel to a distinct diffraction pattern on a CCD array

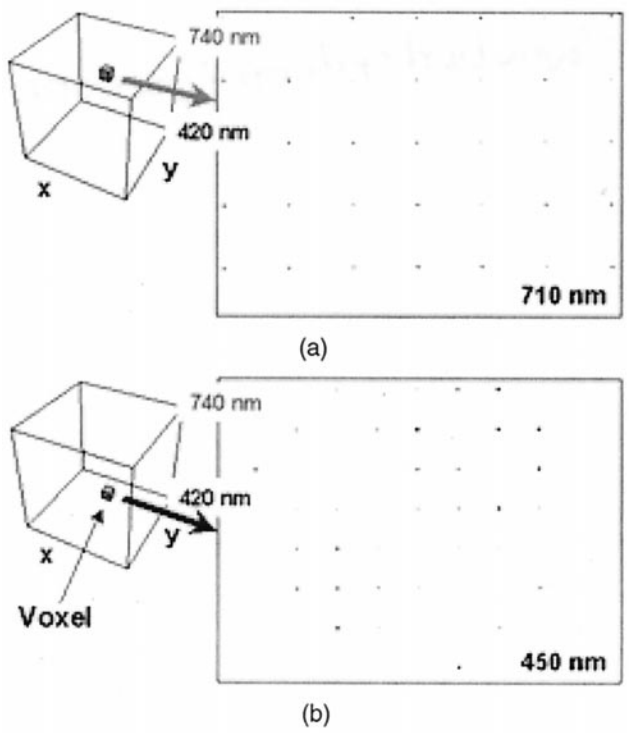

FIGURE 2 Mapping of signal from voxel to imaging array. The signal on the imaging array is distributed in a diffraction pattern that depends on a voxel's (x, y, λ) coordinates in the object cube. Part (a) shows a voxel at a center wavelength of 450 nm and the distribution of that voxel's signal on the imaging array. Part (b) shows a voxel at a center wavelength of 710 nm and the distribution of that voxel's signal on the imaging array.

by means of the CGH disperser. A set of diffraction patterns, such as those shown in Fig. 2, is recorded for all voxels in the object cube during a single integration time. A shift in the center wavelength of a voxel results in the expansion or contraction of the diffraction pattern within the focal plane. A change in the voxel's spatial position results in a corresponding translation of the diffraction pattern across the focal plane. The ensemble of the diffraction patterns associated with each voxel describes the mapping from the three-dimensional (3D) (x, y, λ) object space to the 2D image space (detector array) effected by the CTIS. This mapping can be mathematically inverted to reconstruct an object cube from a raw image.

The zeroth diffraction order image is the result of direct imaging through the CGH disperser without any dispersion (see center field image in Fig. 3). This image therefore represents an undispersed, broadband view of the specimen. Consequently, the zeroth order image can be used to aim and focus the microscope without the need for any data processing. Thus, sample selection and initial positioning information are easily obtained. The higher order images are associated with an increased dispersion, which manifests itself as a radial blur in the higher diffraction orders.

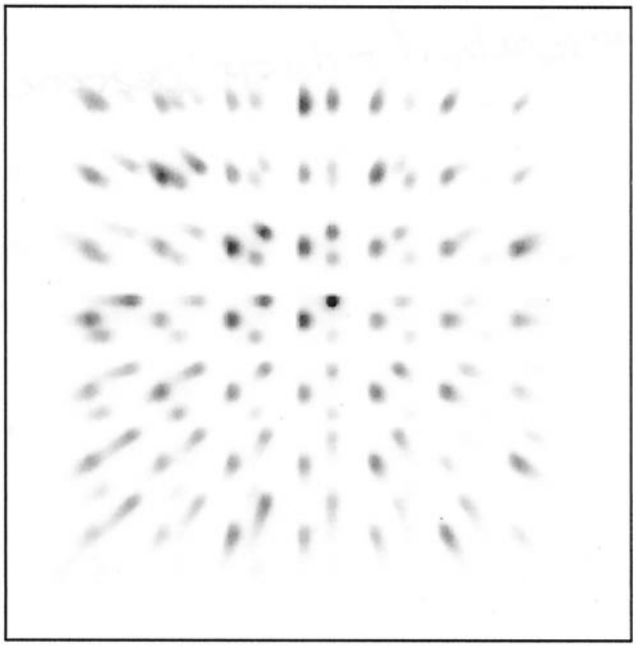

FIGURE 3 A raw image of 15-μm-diameter microspheres with excitation and emission peaks in nanometers at 505/535, 540/560, and 580/605. The image was taken at a magnification of ~320×, using a 40×, NA = 1.3 objective and an 8× imaging eyepiece.

INSTRUMENT MODELING

The CTIS instrument is modeled as a linear imaging system and therefore can be described in terms of linear algebra. The 2D image (Fig. 3) and the 3D object cube are reorganized as vectors $\mathbf{g}$ and $\mathbf{f}$, respectively. These vectors are related to each other by means of a system matrix, denoted by H. The matrix H can be acquired experimentally by recording calibration images, such as those shown in Fig. 2, for every voxel within the object cube (Descour and Dereniak, 1995; Descour et al., 1997b). As a result of the shift-invariance of the CTIS subsystem, only a single calibration image per wavelength band needs to be acquired and recorded (Volin et al., 1998). As unrecorded calibration images are needed during reconstruction of the object cube, the stored calibration images are recalled and shifted to the desired spatial position.

The reconstruction of the 3D object cube is performed using the multiplicative algebraic reconstruction technique (MART). The iterative progression from the kth estimated object cube, $\hat{\mathbf{f}}^k$, to the $(k + 1)$st occurs according to the equation

$$\hat{\mathbf{f}}^{k+1} = \hat{\mathbf{f}}^k \frac{H^T\mathbf{g}}{H^T H\hat{\mathbf{f}}^k}, \tag{1}$$

where T indicates the matrix transpose and $H^T\mathbf{g}$ and $H^T H\hat{\mathbf{f}}^k$ form the backprojection of the collected raw image and the current image estimate, respectively. The multiplications

and divisions are taken to be point-by-point operations (Lent, 1976).

The CTIS belongs to the category of restricted view angles instruments. As such, each voxel of the object cube is viewed through only a limited set of angles corresponding to the limited number of projections on the 2D detector array. As is the case for all instruments within this class, there exist two missing cones of data within the 3D Fourier transform of the object cube (Barrett and Swindell, 1981). This translates into a limitation on the reconstruction of objects whose frequency space representation falls within these missing cones. Such objects include those with little spatial contrast and sharp spectral transitions (Descour and Dereniak, 1995). Placing additional constraints on the reconstruction algorithm can reduce the reconstruction artifacts attributed to objects of this type. These constraints will become essential as we shift from imaging isolated cell populations to imaging confluent monolayers of cells or whole tissue slices.

Reconstruction tests performed in conjunction with a non-imaging reference spectrometer were used to determine the number of iterations yielding the greatest accuracy in the reconstructed spectra. Typically, seven or eight iterations proved optimal. Therefore, the results presented in the next section were obtained after eight (8) iterations of the reconstruction algorithm. Iterations required ~22 s to complete on a 450 MHz Pentium II personal computer for 75 × 75 spatial resolution elements and 30 spectral bands. In our current work, the initial estimate of the object cube, $\hat{\mathbf{f}}^0$, corresponds to a spectrally and spatially uniform field of view. Use of an initial guess that more closely resembles the object would provide a more accurate reconstruction using fewer iterations. This can be accomplished by using an estimate, which is spatially identical to the zeroth order image and spectrally uniform.

In the above model, we have assumed that the light incident on the detector array arises from a single axial slice through the 3D sample (x, y, z). For the types of samples presented here (monolayers of cells and sparse microspheres), the out-of-focus contributions can be reasonably neglected. Extending the applicability of the CTIS to the spectral analysis of multilayer samples will require the development of multispectral deconvolution techniques. The design of a second CTIS system dedicated to 3D (x, y, z) spectral imaging is currently underway.

RESULTS

Resolution of spectral signatures using fluorescent microspheres

A mixture of three 15-μm-diameter microspheres with different fluorescent characteristics was imaged through the CTIS microscope. The raw image shown in Fig. 3 was recorded using a digital scientific camera operating at a frame rate of 15 frames/s and with an integration time of 40 ms. Fig. 4 *a* shows the reconstructed image with pixel locations corresponding to the reconstructed spectra in Fig. 4 b. These spectral curves show the clear spectral separation of the three reconstructed microspheres. The full spectral and spatial information for this image was obtained during a single integration time. The estimated spatial sampling distance between adjacent pixels is 0.7 μm. A raster display of 18 reconstructed spectral images of this sample is shown in Fig. 5. Due to the inherent co-registration of these spectral images, post-processing for correcting pixel alignment is unnecessary. Due to the relatively large fluorescence signal associated with the microspheres, a high degree of temporal resolution also was realized. These results demonstrate the instrument's potential to simultaneously capture the spectral signatures of multiple fluorophores from different regions within the same sample with a relatively high temporal resolution.

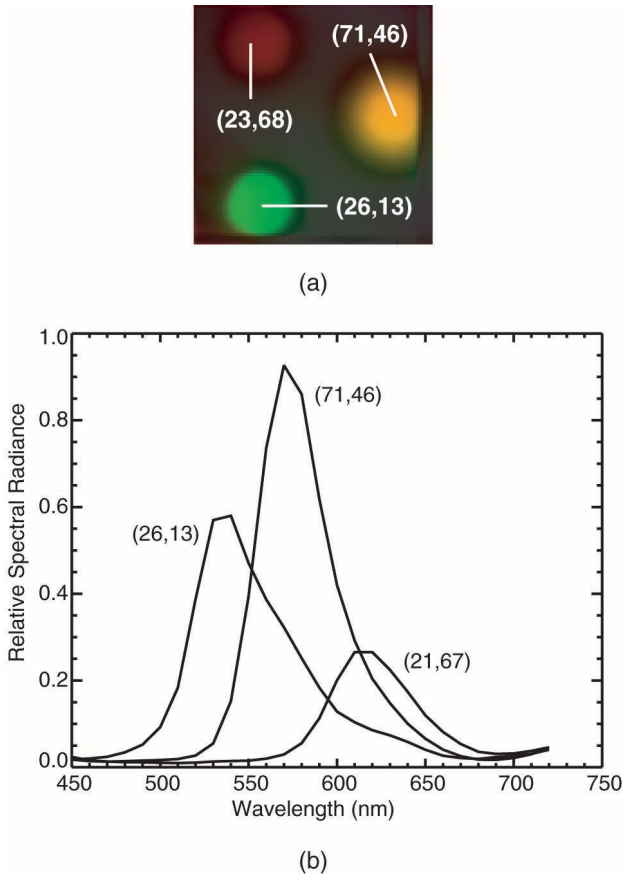

FIGURE 4 (*a*) Reconstructed image of multispectral microspheres. Microspheres are 15 μm in diameter. The dimensions of the reconstructed object cube were 83 × 83 × 31. The spatial sampling between adjacent pixels is 0.7 μm for this image. (*b*) Reconstructed spectra from three different locations within the combination microsphere sample shown in *a*. Eight iterations of the reconstruction algorithm were performed. Each iteration required 17 s on a Pentium II 450 MHz personal computer.

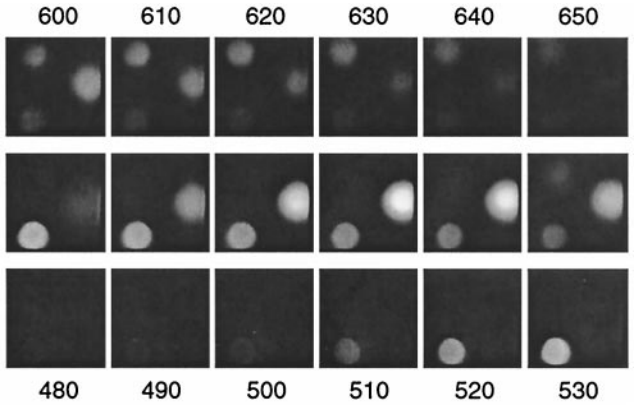

FIGURE 5 Raster display of a subset of spectral images of the combination microsphere sample. Wavelength increases in raster fashion from left to right, bottom to top, in steps of 10 nm. The numbers provided in the above image are wavelengths in nanometers. Note the clear spectral separation of the YG, orange, and red microspheres.

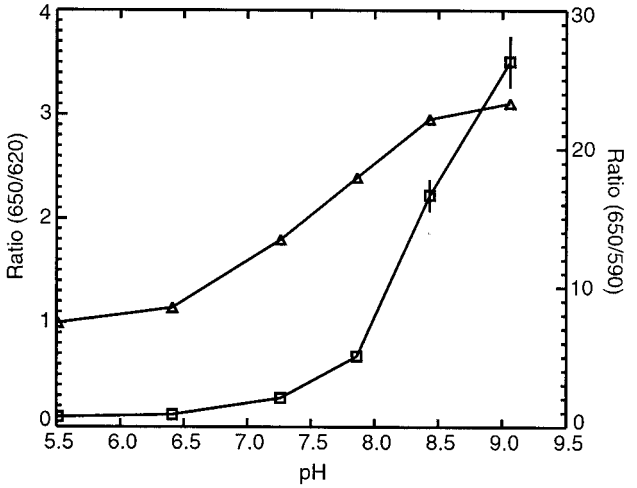

FIGURE 7 Free acid calibration of SNARF-1 generated from ratios of the pH-sensitive wavelengths (650/590). *Squares*, data are means ± standard error of five independent experiments. Ratio of the pH-sensitive wavelength, 650 nm, to the isoemissive wavelength, 620 nm, for a single calibration trial (*triangles*).

Response of SNARF-1 free acid to changes in media pH

SNARF-1 is a molecule whose fluorescence spectrum shifts in response to changes in ambient pH. A calibration of SNARF-1 free acid in an aqueous solution was performed to determine the sensitivity and stability of the CTIS. Reconstructed spectra from images acquired at different pH values and the responses at specific wavelengths are shown in Fig. 6, *a* and *b*, respectively. Calibration curves based on the ratio of fluorescence emission at the ion-sensitive wavelengths (650 nm/590 nm) and the ratio of the SNARF-1 basic peak relative to the isoemissive wavelength (650 nm/620 nm) are shown in Fig. 7. From Fig. 6 *b* it is clear that the fluorescence emission at the isoemissive wavelength is stable, while the emissions at the H^+-sensitive wavelengths change as expected. However, based on the ratio of ion-sensitive wavelengths, the pK_a appears to be shifted to the right (accepted $pK_a \sim 7.6$; Bassnett et al., 1990) with the dye ratio not reaching a maximal value until after a pH of 9.0. This apparent shift in pK_a can be corrected if the signal from an ion-sensitive wavelength is normalized to the fluorescence intensity at the isoemissive point (Fig. 7). The basis for the spurious calibration using the ratio of ion-sensitive wavelengths is the low signal intensity at the

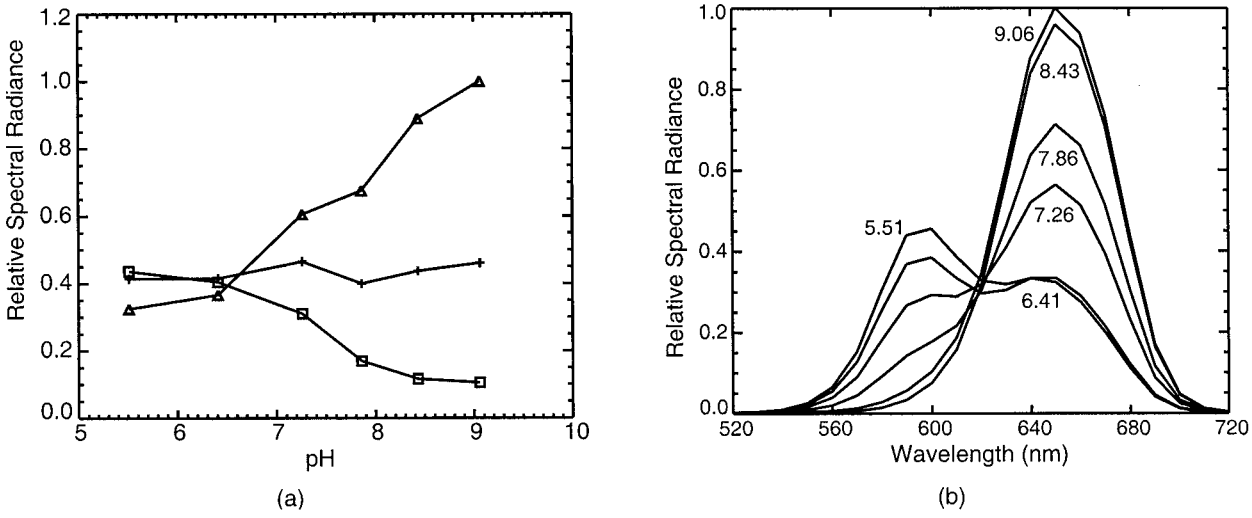

FIGURE 6 (*a*) Reconstructed spectra acquired during a single trial of the free acid calibration of SNARF-1. Each curve corresponds to the average spectrum for different pH solutions. (*b*) Average response of the SNARF-1 at the pH-sensitive wavelengths, 590 nm (*squares*) and 650 nm (*triangles*), and the isoemissive point, 620 nm (*crosses*) during a single calibration trial.

acidic peak (590 nm), which can lead to errors in the ratio at high pH values.

In situ calibration of SNARF-1 loaded into rat insulinoma (RIN) cells

The applicability of the CTIS microscope to standard physiological experiments was demonstrated by recording the response of SNARF-1 to changes in pH in an insulin-secreting rat insulinoma cell line RIN-38 (Clark et al., 1990). SNARF-1 exhibits a distinct shift in its emission spectrum in response to changes in pH within the physiological range of pH values observed within the RIN cells. Raw images were collected using a 12-bit cooled CCD camera with integration times of up to 2 s. A post-reconstruction image of several SNARF-1-loaded RIN cells is shown in Fig. 8. By eliminating the necessity for spectral or spatial scanning, full spectral information is obtained from all cells during a single integration time. This allows for comparison of probe response between individual cells and potentially individual subcellular compartments.

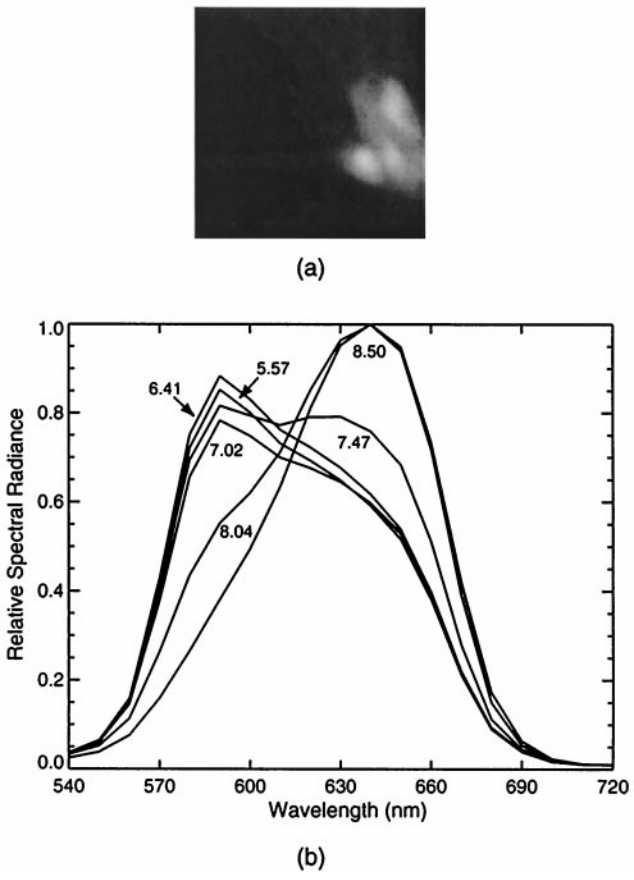

FIGURE 8 (*a*) Post-reconstruction image of several RIN cells loaded with SNARF-1. Eight iterations of the reconstruction algorithm were performed to reconstruct the object cubes (75 × 75 × 30). Each iteration required 22 s on a Pentium II 450 MHz personal computer. (*b*) Reconstructed spectra acquired during a single trial of the in situ calibration of SNARF-1. Each curve corresponds to the average spectrum across an RIN cell in the presence of different pH solutions.

Reconstructed spectra shown in Fig. 9 *a* were obtained by plotting the average fluorescence emission over a 10 μm × 10 μm area of a single cell during the in situ calibration. The spectral shift of the SNARF-1 fluorescence is clearly observed with changing pH. Fig. 9 *a* shows the response at the individual ion-sensitive wavelengths and the isoemissive wavelength. Because the data at all wavelengths are collected simultaneously, issues of co-registration are removed, improving the measurement accuracy when compared to approaches that require filter switching. Ratio data collected during an in situ calibration and averaged for five cells is shown in Fig. 9. As seen with the calibration of the free acid, the pK_a derived from the plot of ion-sensitive wavelengths appears shifted to higher pH values (Fig. 9 *b*). In this case, there was a substantial decrease in dye density between pH 7.5 and 8 shown by the intensity at the isoemissive point. Again, when normalizing the intensity at the basic peak to the response at the isoemissive wavelength, a reasonable calibration curve is obtained. These observations demonstrate the utility of acquiring full spectral data for accurate analysis of probe function.

The functional response of SNARF-1 was analyzed by treating SNARF-1-loaded cells with the weak base NH_4Cl. The responses of four individual cells are shown in Fig. 10. The 640/590 calibration curve shown in Fig. 9 was used to compute the pH values. Addition of NH_4Cl elicits a sudden alkalization of the cytosol followed by recovery to near resting pH. Upon removal of NH_4Cl from the media, NH_4 rapidly exits the cell, causing sudden acidification. Cytosolic pH recovers from this acid load due to the activity of H^+ extrusion mechanisms resident in the cell-limiting membrane. Measured recovery rates are similar to those observed in these cells using a standard spectral imaging microscope (Martinez-Zaguilán et al., 1996a). Notice that resting pH differs between individual cells, and this influences the rate of recovery from the acid load.

CONCLUSIONS

We have presented proof-of-concept imaging results obtained with the CTIS in combination with a commercial inverted fluorescence microscope. The CTIS microscope can simultaneously collect spatial and spectral image data with relatively high spatial and spectral resolution. The current spatial and spectral sampling intervals of the instrument are 1.0 μm and 10 nm, respectively. This level of resolution is adequate to resolve signal responses from multiple fluorescence probes located within individual cells. Two aspects of the current system need further development for standard use in biological imaging. First, the field of view must be increased such that sampling of signal over a wider tissue area can be accomplished. This improvement will require an increase in the number of spatial resolution

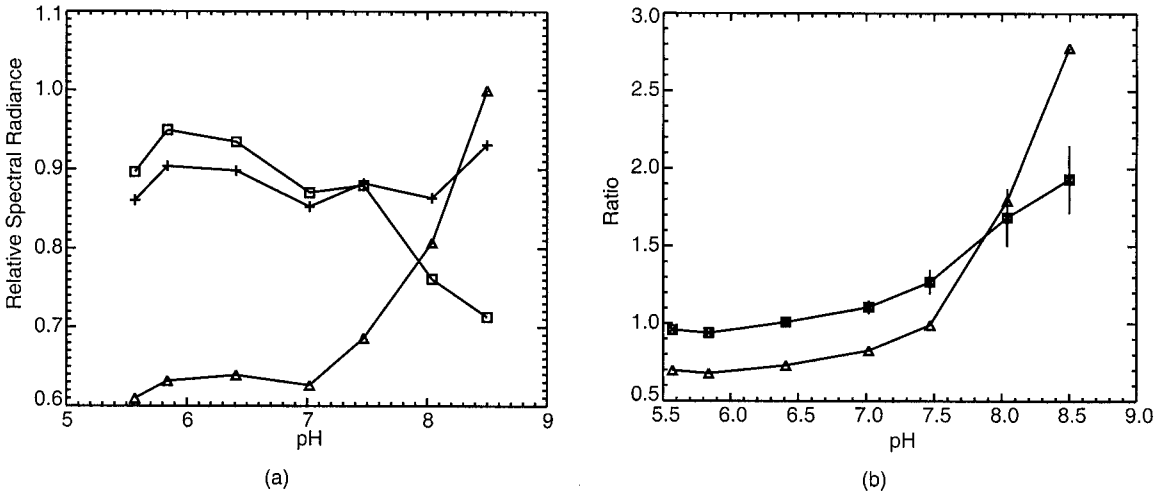

FIGURE 9 (*a*) Average response of the SNARF-1 loaded cells at the pH sensitive wavelengths, 590 nm (*squares*) and 640 nm (*triangles*), and the isoemissive point, 610 nm (*crosses*) during a single calibration trial. (*b*) In situ calibration of SNARF-1 loaded in RIN cells generated from ratios of the pH-sensitive wavelengths (640/590). *Squares*, data are means ± standard error of five independent experiments. Ratio of the pH-sensitive wavelength, 640 nm, to the isoemissive wavelength, 610 nm, for a single calibration trial (*triangles*).

elements beyond the maximum of 83 × 83 reported in this paper. Additionally, increasing the signal-to-noise ratio of the CTIS microscope is required because many functional probes either have relatively low quantum yield or cannot be loaded to a high level without affecting cell function. During preliminary spectral imaging experiments, we determined that the transmission of the combined microscope and spectrometer system (currently ~40%) could be significantly increased with relatively modest modifications. An increase in system transmission will result in an increased signal-to-noise ratio while providing the capability for faster data acquisition. We estimate the total system transmission can be increased by 5–10% by simplifying the optical system, taking advantage of high-efficiency anti-reflection coatings, and redesigning the CGH disperser to maximize its efficiency. These improvements will be addressed in a second generation of the CTIS microscope. The new configuration will use a large-format detector array (2048 × 2048) and revised disperser design, resulting in an increased number of spatial resolution elements to 200 × 200. Therefore, as a consequence of reasonable hardware modifications, simultaneous 2D analysis of multiple probes (cell functions) throughout a heterogeneous sample will be attainable.

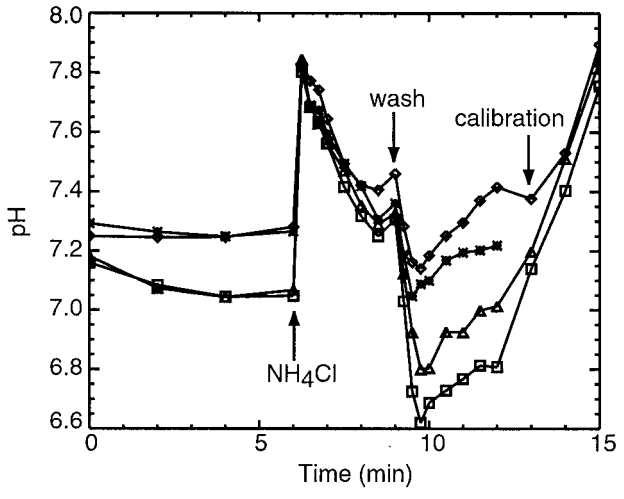

FIGURE 10 The functional responses of four cells loaded with SNARF-1 treated with the weak base NH_4Cl. Plotting symbols denote individual cellular responses within the sample.

The simultaneous spectral and spatial imaging capabilities of the CTIS have the potential to provide an important technological advancement in a range of research areas. For example, the CTIS is an optimal tool for the study of physiological changes in function from populations of cells, which respond heterogeneously. Examples include individual cells within a tissue, such as a liver slice, or a population of isolated cells, such as neuronal cultures. To understand how individual cells respond and how interactions between unique cell types occur, it is critical to simultaneously monitor several functional parameters from many cells. The use of fluorescent reporter compounds provides a tool to evaluate changes in specific functional characteristics, such as ion movements and metabolism. The reporters, however, may not be completely selective, or their signals may be difficult to calibrate. Analysis of contiguously sampled spectra provides a sensitive approach to correct for probe-independent artifacts, dye-dye interactions, and cross-sensitivity between probes (Martinez-Zaguilán et al., 1996b). The CTIS microscope also can be an important tool to study the effects of drugs and toxic agents on the physiology of tissue such as the liver. Because these types of effectors

often elicit changes in many cell functions, the ability to monitor more than one probe simultaneously from unique tissue regions will provide an important technical advance, providing detailed information regarding changes in ion movements (H^+, Ca^{2+}, K^+) and metabolism (O_2, NADH) from cells throughout a functioning hepatic unit, for example.

The CTIS also may be beneficial in clinical diagnosis and disease staging where optical biopsy is providing a less invasive alternative to more traditional approaches. Optical biopsy can be used in conjunction with imaging of either tissue autofluorescence or emission from a fluorescent drug to induce an optical contrast between tumors and the surrounding normal tissue (Sabharwal et al., 1999). Analysis of the fluorophore distribution for normal and tumor tissue provides additional contrast within the spatial FOV, allowing a determination of tumor infiltration. As optical biopsy is often an endoscopic procedure, rapid data acquisition is essential in reducing motion artifacts and for patient comfort. In this respect, the potential high-speed imaging capabilities of the CTIS may prove advantageous (Ford et al., 1999).

The authors thank E. L. Dereniak of the Optical Sciences Center and G. H. Bearman of the Jet Propulsion Laboratory for their support of and assistance with the work presented in this paper. We are also grateful to D. Wilson and P. D. Maker of the Jet Propulsion Laboratory for providing the CGH disperser.

The work presented in this paper was funded in part by the National Science Foundation (Grant DBI-9876717, B.K.F.), the American Diabetes Association (R.M.L.), and the National Institutes of Health (Grant RR14239, to M.R.D. and R.M.L.).

REFERENCES

Barrett, H. H., and W. Swindell. 1981. Radiological Imaging: The Theory of Image Formation, Detection, and Processing. Academic Press, Inc., San Diego; London. 491–493.

Bassnett, S., L. Reinisch, and D. C. Beebe. 1990. Intracellular pH measurement using single excitation-dual emission fluorescent ratios. *Am. J. Physiol. Cell Physiol.* 258:C171–C178.

Clark, S. A., B. L. Burnham, and W. L. Chick. 1990. Modulation of glucose-induced insulin secretion from a rat clonal β-cell line. *Endocrinology.* 127:2779–2788.

Descour, M. R., and E. Dereniak. 1995. Computed-tomography imaging spectrometer: experimental calibration and reconstruction results. *Applied Optics.* 34:4817–4826.

Descour, M. R., C. E. Volin, E. L. Dereniak, K. J. Thome, A. B. Schumacher, D. W. Wilson, and P. D. Maker. 1997b. Demonstration of a high speed non-scanning imaging spectrometer. *Optics Letters.* 22: 1271–1273.

Descour, M. R., C. E. Volin, T. M. Gleeson, E. L. Dereniak, M. F. Hopkins, D. W. Wilson, and P. D. Maker. 1997a. Demonstration of a computed-tomography imaging spectrometer using a computer-generated hologram disperser. *Applied Optics.* 36:3694–3698.

Eng, J., R. M. Lynch, and R. S. Balaban. 1989. Nicotinamide adenine dinucleotide fluorescence spectroscopy and imaging of cardiac myocytes. *Biophys. J.* 55:621–630.

Ford, B. K., C. E. Volin, A. R. Rouse, R. M. Lynch, A. F. Gmitro, G. H. Bearman, and M. R. Descour. 1999. Video-rate spectral imaging system for fluorescence microscopy. *In* Systems and Technologies for Clinical Diagnostics and Drug Discovery II. G. E. Cohn, John C. Owicki, editors. *SPIE Proc.* 3603:216–226.

Garini, Y., A. Gil, I. Bar-Am, D. Cabib, and N. Katzir. 1999. Signal to noise analysis of multiple color fluorescence imaging microscopy. *Cytometry.* 35:214–226.

Haugland, R. 1999. Handbook of Fluorescent Probes and Research Chemicals, 7th Ed. Molecular Probes, Inc. Eugene, OR.

Lent, A. 1976. A convergent algorithm for maximum entropy image restoration. *In* Image Analysis and Evaluation. Rodney Shaw, editor. SPSE Conference Proceedings, July 19–23; 1976, Toronto, Canada. 249–257.

Martinez-Zaguilán, R., M. W. Gurulé, and R. M. Lynch. 1996a. Simultaneous measurement of intracellular pH and Ca^{2+} in insulin-secreting cells by spectral imaging microscopy. *Am. J. Physiol. Cell Physiol.* 39:C1438–C1446.

Martinez-Zaguilán, R., G. Parnami, and R. M. Lynch. 1996b. Selection of ion indicators for simultaneous measurement of pH and Ca^{2+}. *Cell Calcium.* 19:337–349.

Mason, W. T., editor. 1999. Fluorescent and Luminescent Probes for Biological Activity: A Practical Guide for Quantitative Real-Time Analysis. Academic Press, London; San Diego.

Mooney, J. M., V. E. Vickers, M. An, and A. K. Brodzik. 1997. High-throughput hyperspectral infrared camera. *J. Opt. Soc. Am. A.* 14: 2951–2961.

Morris, H. R., C. C. Hoyt, and P. J. Treado. 1994. Imaging spectrometers for fluorescence and Raman microscopy—acoustooptic and liquid crystal tunable filters. *Appl. Spectrosc.* 48:857–866.

Ornberg, R. L., B. M. Woerner, and D. A. Edwards. 1999. Analysis of stained objects in histological sections by spectral imaging and differential absorption. *J. Histochem. Cytochem.* 47:1307–1313.

Richmond, K. N., S. Burnite, and R. M. Lynch. 1997. Oxygen sensitivity of mitochondrial metabolic state in isolated skeletal and cardiac myocytes. *Am. J. Physiol. Cell Physiol.* 273:C1613–C1622.

Sabharwal, Y. S., A. R. Rouse, L. Donaldson, M. F. Hopkins, and A. F. Gmitro. 1999. Slit-scanning confocal microendoscope for high resolution in vivo imaging. *Applied Optics.* 38:7133–7144.

Schröck, E., S. du Manoir, T. Veldman, B. Schoell, J. Wienberg, M. A. Ferguson-Smith, Y. Ning, D. H. Ledbetter, I. Am-Bar, D. Soenksen, Y. Garini, and T. Ried. 1996. Multicolor spectral karyotyping of human chromosomes. *Science.* 273:494–497.

Volin, C. E., B. K. Ford, M. R. Descour, J. P. Garcia, P. D. Maker, and G. H. Bearman. 1998. High-speed spectral imager for imaging transient fluorescence phenomena. *Applied Optics.* 37:8112–8119.

Wachman, E. S., W. H. Niu, and D. L. Farkas. 1997. AOTF microscope for imaging with increased speed and spectral versatility. *Biophys. J.* 73: 1215–1222.

Wang, X. F., and B. Herman. 1996. Fluorescence Imaging Spectrometry and Microscopy. John Wiley and Sons, Inc., New York.

Wiegmann, T. B., L. W. Welling, D. M. Beatty, D. E. Howard, S. Vamos, and S. J. Morris. 1993. Simultaneous imaging of intracellular [Ca^{2+}] and pH in single MDCK and glomerular epithelial cells. *Am. J. Physiol. Cell Physiol.* 265:C1184–C1190.

Zangaro, R. A., L. Silveira, Jr., R. Manoharan, G. Zonios, I. Itzkan, R. R. Dasari, J. Van Dam, and M. S. Field. 1996. Rapid multiexcitation fluorescence spectroscopy system for in vivo tissue diagnosis. *Applied Optics.* 35:5211–5219.

Zeng, H. S., A. Weiss, C. MacAulay, and R. W. Cline. 1999. System for fast measurements of in vivo fluorescence spectra of the gastrointestinal tract at multiple excitation wavelengths. *Applied Optics.* 38:7157–7158.